Nano Research

Open Access

Research Article

Green ionic metal-organic frameworks as nanocatalysts for CO_2 fixation

Nuria Martín[§] ✉, Miguel Maireles-Porcar[§], Julián Sánchez Velandia, Belén Altava, Francisco G. Cirujano ✉, and Eduardo García-Verdugo ✉

Departamento de Química Inorgánica y Orgánica, Universidad Jaume I, Av. Sos Baynat, s/n, Castelló de la Plana, Castellón 12071, Spain
[§] Nuria Martín and Miguel Maireles-Porcar contributed equally to this work.

Cite this article: *Nano Research*, **2025**, *18*, 94907069. https://doi.org/10.26599/NR.2025.94907069

ABSTRACT: Co, Ni, and Zn iso-reticular coordination polymers of 2,5-dihydroxyterphthalic acid (H_2dot) can be rapidly obtained under room temperature and aqueous conditions using either sodium or ammonium hydroxide as the bases to deprotonate the linker. The use of metal bromides and tetrabutylammonium hydroxide (TBAOH) as the base allows the green synthesis of ionic metal-organic frameworks (MOFs), characterized by X-ray diffraction (XRD), Fourier transform infrared (FTIR), scanning electron microscopy (SEM), thermo gravimetric analysis (TGA), H-nuclear magnetic resonance (NMR), elemental analysis, and X-ray photoelectron spectroscopy (XPS), and employed in the pressure, solvent, and additive-free CO_2 fixation to epoxides by its cycloaddition to epichlorohydrin, exhibiting a cooperative behavior between the MOF and the ionic liquid formed within the framework, achieving TONs of the confined tetrabutylammonium bromide (TBABr) up to 700.

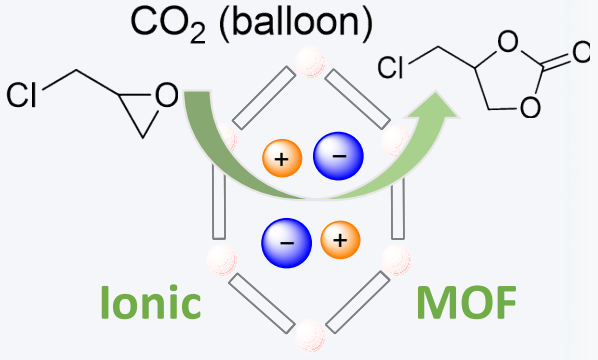

KEYWORDS: metal-organic frameworks (MOFs), ionic liquids, heterogeneous catalysis, CO_2 conversion

1 Introduction

The ordered atomic isolation of organic and/or metal active sites at the supramolecular metal-organic framework (MOF), as well as a facilitated diffusion of reagents and products through the tunable and regular pores is key for adsorption and catalysis applications [1, 2]. In particular, their porosity ensures the rational incorporation of extra-framework catalytically active species, such as ionic liquids (ILs), composed of bulky ions with low melting points and vapor phase [3]. To tackle their high viscosity, poor substrate diffusion and complicated product separation (which often gets contaminated with ionic liquid), supports of the IL phase, such as MOFs can be employed, which can also enhance their activity and stability after inmobilization [4, 5]. Lewis acid MOFs and nucleophilic ionic liquids have been combined to promote the cycloaddition of CO_2 into epoxides to give cyclic carbonates [6]. Both the use of renewable glycerol-derived epichlorohydrin epoxides and greenhouse and pollutant CO_2, allows for the obtention of bio-based plastics (i.e. polycarbonates) with a lower carbon footprint than fossil-based plastics and offers the possibility of recycling and biodegradation [7, 8].

Earth-abundant first-row cobalt or zinc centers stabilized with macrocyclic salen and bis(phenolate) ligands exhibit high catalytic activity in the reaction of CO_2 with epoxides, achieving TONs of ca. 50 (for the tetra butyl ammonium bromide co-catalyst) or 200 (considering only the zinc complex) [9, 10]. Similar metal phenolate/carboxylate moieties are extended in the three-dimensional (3D) framework of the metal-dioxyterephthalate coordination polymer MOF-74, also known as CPO-27 (abbreviation of coordination polymer) or simply M_2(dot), with a high density of open metal sites at the one-dimensional (1D) hexagonal channels (pores) of 11 Å [11, 12]. The architecture of M_2(dot) is based on carboxylate and phenolate groups at the 2,5-dihydroxyterephthalic acid (H_4dot) linker, that coordinate divalent metal cations after the deprotonation of the more acidic carboxylate group first and the phenolate group next. This MOF has been traditionally prepared from the corresponding divalent metal ions and organic linker under solvothermal conditions, requiring large

Received: August 2, 2024; **Revised:** September 23, 2024
Accepted: October 11, 2024

✉Address correspondence to Nuria Martín, numartin@uji.es; Eduardo García-Verdugo, cepeda@uji.es; Francisco G. Cirujano, cirujano@uji.es

volumes of organic solvent (N,N-dimethyl formamide (DMF)), high temperatures (> 100 °C), and long reaction times (see top part of Scheme 1).

To achieve cost-efficient heterogeneous catalysts for CO_2 fixation, greener synthetic methods of such nanomaterials are required [13]. At the same time, there is an urgent need to improve the catalytic performance of current MOF-based systems. This can be achieved by reducing the amount of MOF (< 1.5%) and the co-catalysts tetrabutylammonium bromide and tetrabutylammonium bromide (TBABr) (< 5%) and CO_2 (< 12 bar) that are currently used [14]. Herein we propose a new synthetic method (different from classic ionothermal synthesis, wet impregnation, or ship-in-a-bottle covalent/electrostatic grafting) to address both the MOF synthesis greenness and incorporation of IL within the same ionic MOF. On the one hand, we propose the use of strong bases in water (as an alternative to toxic and expensive organic solvents) to deprotonate both groups in the dot linker and form the M_2(dot) MOF by self-assembly/precipitation in the presence of the corresponding metal (M = Zn, Co, and Ni), leading to green M-MOF-74, which has only been reported for the highly stable zinc MOF (and not for Co or Ni isoreticular ones) [15–18]. On the other hand, we propose for the first time the use of organic bases i.e., tetrabutylammonium hydroxide (TBAOH) leading to TBA_4(dot) upon linker deprotonation and metal bromides for the *in-situ* formation and confinement of ionic liquids together with the MOF, thus having a single IL-MOF nucleophilic/Lewis acid multifunctional material. This strategy could lead, in principle, to the simultaneous generation of the M_2(dot) and the TBABr ionic liquid within the MOF structure under one-pot one-step mild room temperature conditions upon the addition of a water solution of MBr_2 (Scheme bottom part of Scheme 1 and left part of Scheme 2).

2 Results and discussion

2.1 Ionic MOF synthesis and characterization

Two different methodologies were assessed for the aqueous room temperature preparation of the M_2(dot) MOFs: (1) using 4 equivalent sodium hydroxide with respect to the linker (with

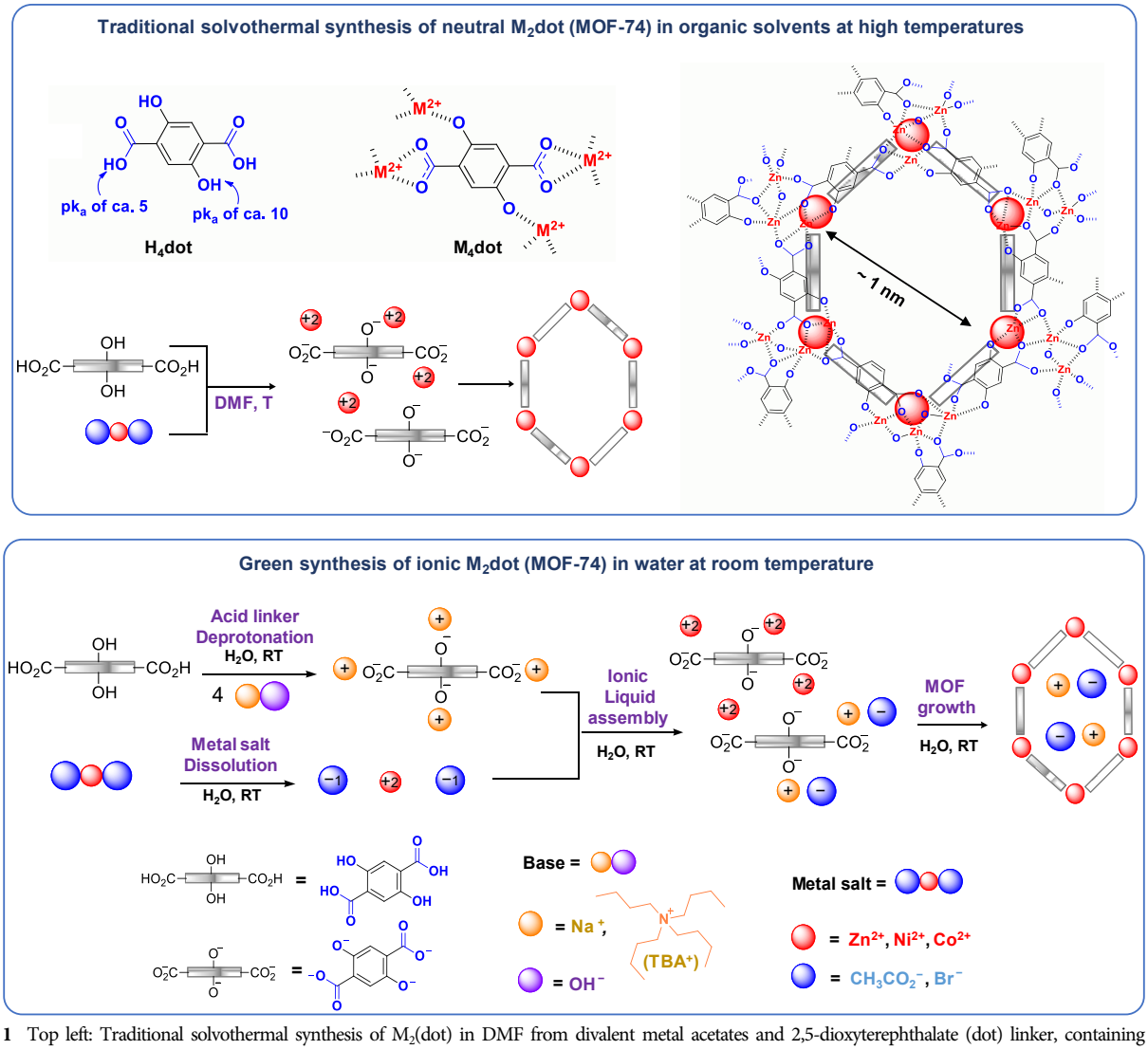

Scheme 1 Top left: Traditional solvothermal synthesis of M_2(dot) in DMF from divalent metal acetates and 2,5-dioxyterephthalate (dot) linker, containing two O-anchoring points (phenol and carboxylic acid). Top right: SBUs and 1D hexagonal nano-channel in M_2(dot) formed upon deprotonation and coordination with the metal ions. (bottom) One-pot synthesis of IL-MOF nanocatalysts under aqueous, ambient conditions using different divalent metals (M = Co^{2+}, Ni^{2+}, or Zn^{2+}) and organic (TBAOH) or inorganic (NaOH) bases for the deprotonation of H_4dot.

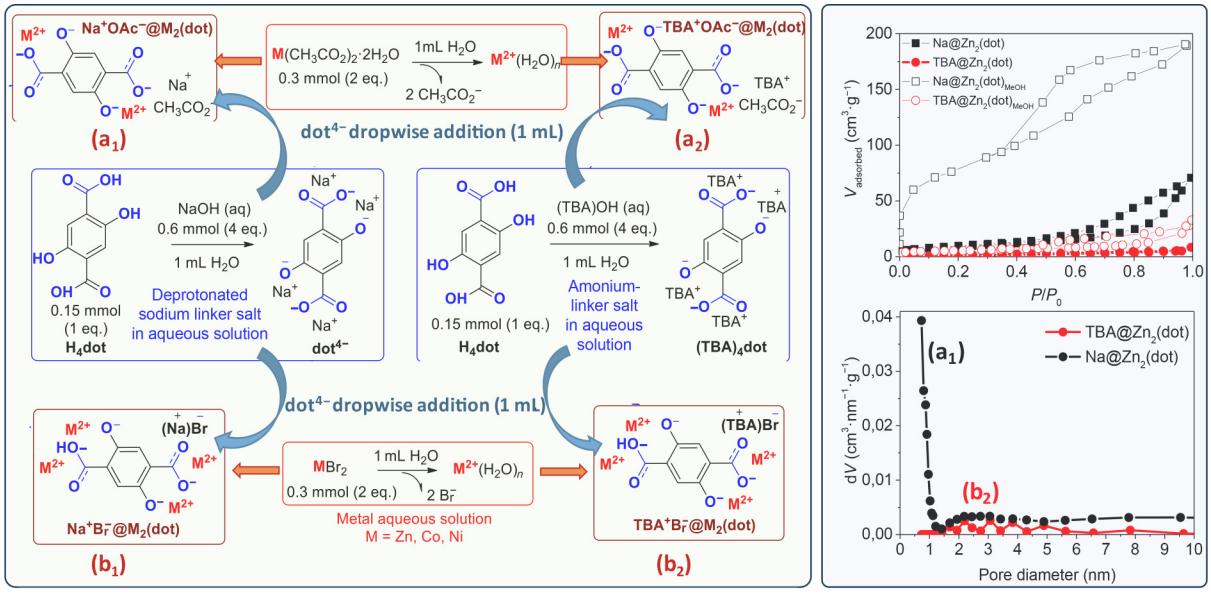

Scheme 2 Left part: (a) MOF-74 (NaOAc@M_2(dot) or simply Na@M_2(dot) in the rest of the text) and MOF-74-ionic liquid composite (TBAOAc@M_2(dot)) synthesis from aqueous solutions of metal acetates and 2,5-dihydroxyterephthalic acid (H_4dot) via NaOH (a_1) or TBAOH (a_2) deprotonation under room temperature conditions. (b) MOF-74 (NaBr@M_2(dot)) and MOF-74-ionic liquid composite (TBABr@M_2(dot) or simply TBA@M_2(dot) in the rest of the text) synthesis from aqueous solutions of metal bromides and 2,5-dihydroxyterephthalic acid (H_4dot) via NaOH (b_1) or TBAOH (b_2) deprotonation and *in situ* ionic liquid formation/encapsulation (a_2) and (b_2) under room temperature conditions. Right part: N_2-physisorption isotherms (top) and pore size distribution (bottom) of the most crystalline and stable Na@Zn_2(dot) and TBA@Zn_2(dot) samples before (filed dots) and after (empty dots) activation in methanol for one week.

4 protons in its structure) deprotonation base (Schemes 2(a_1) and 2(b_1)), or (2) using 4 eq. of tetrabutylammonium hydroxide as the base and also incorporating ionic liquid moieties during the MOF synthesis (Schemes 2(a_2) and 2(b_2)). In the second scenario, it is possible to enhance the encapsulation of ammonium salts by exchanging the Br^- from the metal bromide precursor of the MOF with OH^-, sourced from the ammonium hydroxide base used to deprotonate the linker. This process results in the formation of novel ionic MOFs (Scheme 2(b_2)). Here, we will focus specifically on the synthesis processes described in parts of Schemes 2(a_1) and 2(b_2), with the resulting materials referred to as Na@M_2(dot) and TBA@M_2(dot), respectively. The lower surface area (7 vs. 33 $m^2 \cdot g^{-1}$), pore volume (0.02 vs. 0.12 $cm^3 \cdot g^{-1}$), and higher pore size (2.4 vs. 0.7 nm) of the most robust ionic vs. neutral Zn-MOF, respectively, suggest the confinement of the ionic liquid within the MOF (see right part of Scheme 2). After soaking the materials in methanol for one week at room temperature, followed by thermal activation at 100 °C for one day, the porosity increases to approximately 250 $m^2 \cdot g^{-1}$ for Na@Zn_2(dot) and 20 $m^2 \cdot g^{-1}$ for TBA@Zn_2(dot). Similarly, the pore volume increases to around 0.3 and 0.05 $cm^3 \cdot g^{-1}$ for Na@Zn_2(dot) and TBA@Zn_2(dot), respectively.

The ^{1}H-NMR analysis of the liquid reveals slight leaching of TBABr from the MOF, with less than 1% by weight of TBABr being released. Specifically, only 0.74 mmol of TBABr was leached from 100 mg of the MOF TBA@Zn_2(dot), (1.68 wt.% N) in 3 mL of methanol (see Fig. S1 in the Electronic Supplementary Material (ESM)), further demonstrating the strong confinement of TBABr within the MOF structure. The X-ray diffraction (XRD) pattern of the methanol-activated TBA@Zn_2(dot) material (see Fig. S2 in the ESM) shows peaks more similar to those of the non-activated Na@Zn_2(dot) material, but slightly shifted towards higher angles. This shift suggests a minor contraction of the unit cell, likely due to the partial leaching of TBABr.

In general, the neutral and ionic MOFs (independent of the base employed for the RT aqueous linker deprotonation) exhibited an XRD pattern like that of the reported M_2(dot) MOFs obtained by solvothermal methods (compare predicted and experimental patterns in Fig. 1(a)). Two main peaks are observed, corresponding to the (110) and (300) planes at ca. 6.7° and 11.7°, respectively. The broader peaks of Co_2(dot) and Ni_2(dot) materials with respect to the Zn-containing ones might be a result of their smaller particle size as described for other synthesis methods [19]. Zn_2(dot) seemed to crystalize better than Co_2(dot) and Ni_2(dot) and resulted in a larger crystal size due to better nucleation and growth (see Table S1 in the ESM). Applying the Scherrer equation to the XRD peak corresponding to the (110) plane [15], the crystallite size estimated was ca. 70, 10, and 20 nm for Zn_2(dot), Ni_2(dot), and Co_2(dot) (see Table S1 in the ESM).

Scanning electron microscopy (SEM) and transmission electron microscopy (TEM) images indicate a much larger size (ca. 0.5 × 1 μm) for Na@Zn_2(dot), exhibiting defined facets and edges (see Fig. 1(d) and Figs. S3(a)–S3(c) in the ESM). TEM images indicated particle size decrease depending on the cation of the base employed in the deprotonation (compare top and bottom images in Fig. 1(d) and Fig. S3 in the ESM). Whereas in the case of using small and hard cations such as Na^+, larger crystal aggregates are obtained (top part of Fig. 1(d) and Figs. S3(a) and S3(b) in the ESM), in the case of employing softer and bulkier organic cations (e.g. TBA^+) crystals of smaller size and better dispersed are observed (bottom part of Fig. 1(d) and Figs. S3(c) and S3(d) in the ESM). This suggests a geometric-directing effect that differs when using small inorganic cations with respect to larger organic cations. Beside changes in crystal size, the (110) plane shifts to lower diffraction angles (0.16°) in the case of the Zn MOF when using TBAOH (TBA@Zn_2(dot)) with respect to NaOH (Na@Zn_2(dot)) as a linker deprotonating agent. This suggests the expansion and/or changes (see new diffraction signals at 2θ = 6°–9° in Fig. 2(a), top part) of the crystal unit cell having the bulky TBA species within the framework (see the plugging of the MOF pores by TBABr in Scheme 2, right part),

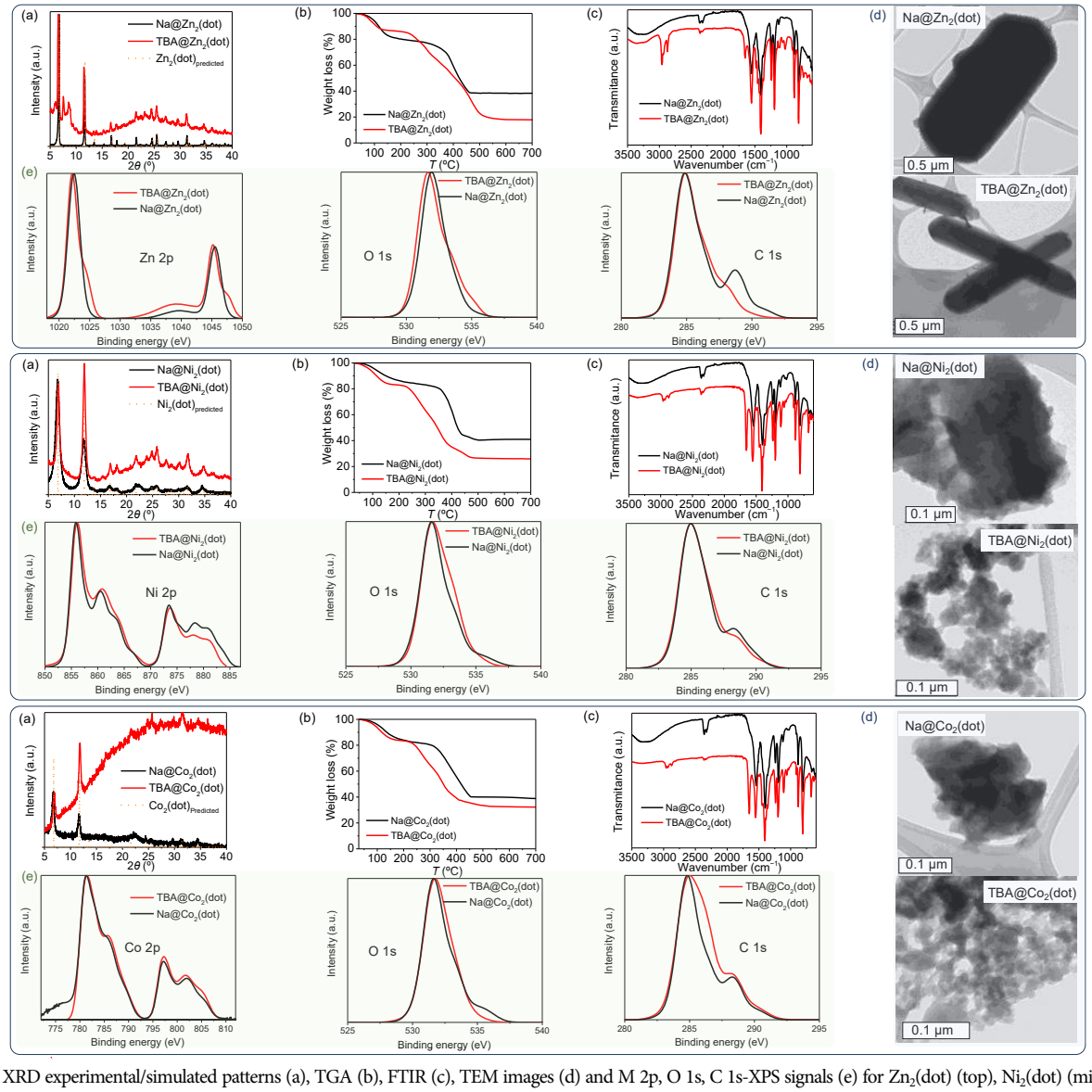

Figure 1 XRD experimental/simulated patterns (a), TGA (b), FTIR (c), TEM images (d) and M 2p, O 1s, C 1s-XPS signals (e) for Zn_2(dot) (top), Ni_2(dot) (middle), and Co_2(dot) (bottom) prepared from $M(OAc)_2$ and Na_4(dot) (black line) or MBr_2 and TBA_4(dot) (red line), respectively.

which is also confirmed by thermo gravimetric analysis (TGA) and Fourier transform infrared (FTIR) analysis of the samples (see Figs. 1(b) and 1(c)).

TGA indicates a large amount of mass corresponding to organic compounds (68% vs. 42%) in TBA@Zn_2(dot) with respect to Na@Zn_2(dot) (see Fig. 1(b), top part). The TBA-related species uptake resulted in 26 wt.% (Zn-MOF), 12 wt.% (Ni-MOF), and 5 wt.% (Co-MOF) organic mass excess in TBA@M_2(dot) with respect to Na@M_2(dot) samples. The inverse trend between ammonium bromide uptake and cation size suggests a better interaction of the large Br^- anions with softer and bigger Lewis acid cations, such as Zn^{2+}. The mass percentage attributed to the inorganic component of the MOF (after heating at 600 °C) is close to the theoretical ZnO present in Zn_2(dot) when NaOH was employed (Table S2 in the ESM), but lower when the MOF is grown in TBAOH (38% vs. 18%, respectively). In the case of TBA@Zn_2(dot), the metal content decreases to half of the value (ca. 14%) with respect to Na@Zn_2(dot) (ca. 30%), while less decrease is found for Na@Ni_2(dot) vs. TBA@Ni_2(dot) (ca. 32% vs. 20%, respectively) and Co@Zn_2(dot) vs. Co@Zn_2(dot) (ca. 31% vs. 25%, respectively), in line with their lower TBABr uptake with respect to the Zn-MOF system.

The higher intensity of the FTIR signal at ca. 2950 cm^{-1} (attributed to the C–H stretching of the butyl chains from TBA) in the TBA@Zn_2(dot) further confirms its higher uptake (see Fig. 1(c)). The signal at ca. 1650 cm^{-1} appearing in the TBA-containing material is similar to that of TBABr and slightly higher than that of TBA_4(dot) linker salt (ca. 1624 cm^{-1}), as shown in Fig. S4 in the ESM. Moreover, the incorporation of this ionic liquid into the MOF was confirmed by digesting the solid in a HCl/dimethylsulfoxide (DMSO) solution and quantifying the butyl signals of the ionic liquid vs. the benzene ring signal of the linker. NMR indicating an excess of 7:1 (TBA:dot) in the Zn_2(dot) MOF (see Fig. S5 in the ESM). However, we expect the results of elemental analysis to be more accurate due to the limited solubility of the MOF linker. Besides, for acid-digested Co and Ni MOFs, the liquid ^{1}H-NMR analysis did not provide information due to the paramagnetic nature of these metals. However, elemental analysis

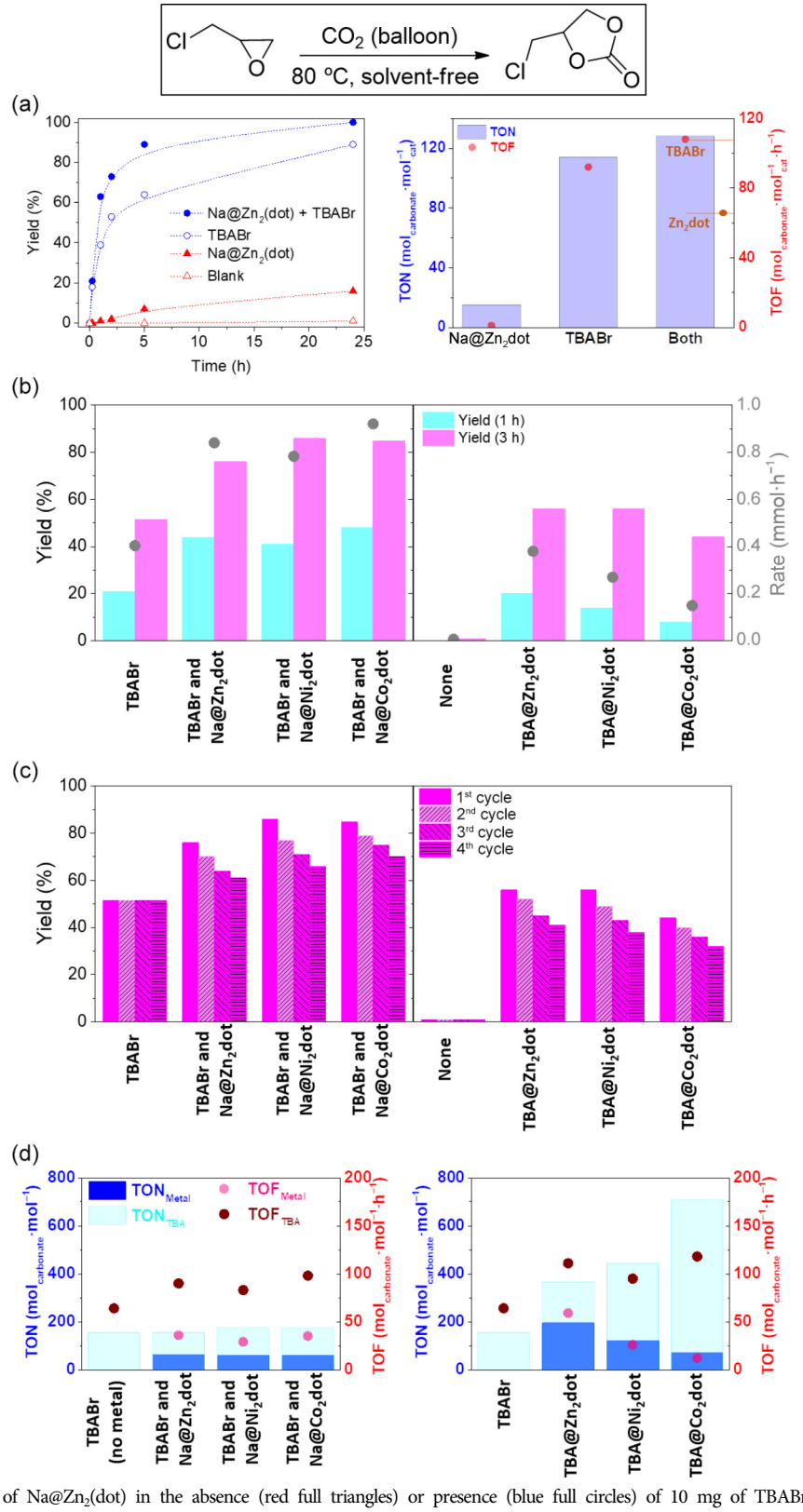

Figure 2 (a) Kinetic profile of Na@Zn_2(dot) in the absence (red full triangles) or presence (blue full circles) of 10 mg of TBABr (0.5 mol%), 6.37 mmol of epichlorohydrin, 10 mg of MOF catalyst (0.7 mol% Zn), 80 °C, CO_2 balloon (1 bar) and 450 rpm. TON and TOF values are obtained from the ratio of mol of product divided by the mol of metal (Na@Zn_2(dot)) or mmol of N (TBABr) or both (Na@Zn_2(dot) + TBABr) after 24 and 0.5 h, respectively. (b) Yield of cyclic carbonate (left axis) after 1 h (blue) and 3 h (magenta) and reaction rate estimated at 1 h of reaction (grey points at right axis). (c) As-prepared and recycled Na@M_2dot and TBA@M_2dot samples after 3 h of reaction using no additional TBABr co-catalyst in the recycles. (d) TON (after 3 h of reaction) and TOFs (after 1 h of reaction) were calculated from the cyclic carbonate yield considering either the metal (calculated from TGA, dark blue bars and light red dots) or TBA (from N content provided by elemental analysis, light blue bars and dark red dots) as the active sites when using 5.7 mmol epichlorohydrin and 15 or 9 mg of Na@M_2(dot) or TBA@M_2(dot), respectively (left part). For TBABr, 0.3% mol with respect to the epoxide was employed (right part).

(see Table S3 in the ESM) indicates an inferior nitrogen weight percentage, increasing in the order ca. 0.07 $mmol_{TBA}·g^{-1}$ (TBA@Co_2(dot)) < ca. 0.93 $mmol_{TBA}·g^{-1}$ (TBA@Ni_2(dot)) < ca. 1.21 $mmol_{TBA}·g^{-1}$ (TBA@Zn_2(dot)).

The X-ray photoelectron spectroscopy (XPS) analysis of metal, oxygen, and carbon signals of the three MOF samples, is represented in the left, middle, and right parts of Fig. 1(e), respectively (also refer to Figs. S6–S8 and Tables S4–S8 in the ESM). The binding energy of the electrons in the metal increases from cobalt (780–805 eV) to nickel (ca. 855–885 eV) and then to zinc (1020–1040 eV), in line with its electronegativity (see the left part of Fig. 1(e) and Figs. S6–S8(a) in the ESM). Some charge donation from the bromine ions to the zinc atoms (increasing the electron density) might occur as the Zn 2p binding energy slightly decreases (by *ca.* 0.3 eV) for TBA@Zn_2(dot) with respect to Na@Zn_2(dot). The middle part of Fig. 1(d), shows that the O 1s signal has a larger proportion of the shoulder at 535.2 eV (see also the O $1s_D$ in Table S4 in the ESM) in the Ni(dot)$_2$ and Co(dot)$_2$ (ca. 7.5% and 7.8%, respectively) with respect to the Zn(dot)$_2$ (ca. 2.3%). This may be associated with free carboxylic acid (or phenol) –CO–H groups not coordinated to the metal sites (O-related point defects), leaving undercoordinated metal sites with Lewis acid character upon the hydrolysis of the metal-carboxylate and/or metal-phenolate coordination bonds [20]. Indeed, the Ni $2p3_A$ component at 855.5 eV may be a result of NiO_4 defect sites [21], in line with both the smaller particle size and the harder acid nature (high charge/ size ratio) of Ni and Co MOFs with respect to Zn (Tables S7 and S8 in the ESM). In the case of the ionic zinc MOFs, which presents a higher uptake of TBABr with respect to Ni and Co-MOFs, the number of O-defects also increases for TBA@Zn_2(dot) with respect to Na@Zn_2(dot), as shown in Fig. 2(b). Moreover, there is a correlation between particle size (see Fig. 1(d) and Table S1 in the ESM) and defect content, since TBA@Zn_2(dot) crystals are smaller (and more defective) than Na@Zn_2(dot), and both Na@Ni_2(dot) and Na@Co_2(dot) are smaller (and more defective) than Na@Zn_2(dot). Regarding the C 1s XPS signals (see right part of Fig. 1(d)), it is worth mentioning that the O–C=O (288.7, 288.3, and 288.4 eV for Zn, Ni, and Co-MOF-74, respectively) vs. C–C (284.8 eV for all three MOFs) contributions are lower for TBA@Zn_2(dot) with respect to Na@Zn_2(dot), suggesting a possible interaction between the carbonyl/oxo groups and the TBA (see also the changes in the C=O band at ca. 1600 cm^{-1} of the TBA-containing MOF in Fig. 1(c)).

2.2 Catalytic performance of the ionic MOFs in the CO_2 cycloaddition to epichlorohydrin

Previously reported Na@Zn_2(dot) prepared at room temperature, aqueous conditions were tested as catalysts in the presence and absence of TBABr co-catalyst (0.5 mol% with respect to epichlorohydrin) in the CO_2 (balloon) cycloaddition to epichlorohydrin (0.7 mol% of Zn) at 80 °C, resulting in the full conversion of epichlorohydrin to the cyclic carbonate in less than 24 h (see Fig. 2(a)), under milder conditions than those previously reported for this MOF [14, 20].

The cyclic carbonate product formation was followed by FTIR (see C=O vibration band at 1797 cm^{-1} in Figs. S9 and S10 in the ESM) using a calibration curve. Specifically, we have considered the cyclic carbonate yield after 1 h of reaction, determined from the calibration curve correlating the FTIR area of the carbonate band of the product at 1800 cm^{-1} and the ^{1}H-NMR (measured in $CDCl_3$) area of the proton bonded to the asymmetric carbon (see Fig. S9 in the ESM).

Figure 2(b) shows that the combination of Na@Zn_2(dot) with TBABr (named as "both" in the graph) outperforms the use of sole TBABr or Na@Zn_2(dot) in terms of activity (see Tables S9 and S10 in the ESM), with a turnover frequency (TOF) of 108 h^{-1} (for the Na@Zn_2(dot)-TBABr combination) vs. 92 h^{-1} (for TBABr) or only 1 h^{-1} for Na@Zn_2(dot). The TOFs were calculated for conversions of epichlorohydrin lower than 20% and considering either the mols of metal (for Na@Zn_2(dot)) or TBABr employed (for TBABr or both Na@Zn_2(dot) and TBABr). Indeed, the TON (calculated as mols of carbonate divided by mols of Zn) is higher (TON = 128) in the presence of the Zn_2(dot)-TBABr combination (obtained with the mols of TBABr used) with respect to using just Zn_2(dot) (TON = 15) or TBABr (TON = 114), obtained considering the mols of TBABr. Thus, a synergic or cooperative effect between the Zn_2(dot) and the TBABr may occur. These values are higher than those reported for the benchmark Zn-MOF-74 prepared under solvothermal conditions [14], using 1.5 mol% Zn, 5 mol% TBABr, 12 bar of CO_2 and room temperature conditions (with reported TON = 65 and TOF = 3 h^{-1}). It is worth mentioning that the Na@Zn_2(dot) green-synthesized MOF (Scheme 2(a_1)) in the absence of any additive and/or co-catalyst can catalyze the reaction (with respect to the blank reaction in the absence of any catalyst), further confirming the role of the MOF activating the CO_2 and epoxide at the base oxygen (from TBAOH-deprotonated phenolate and carboxylate groups) and acid metal sites, respectively [22–24]. Indeed, when bubbling CO_2 into an aqueous solution of TBA_4dot, the formation of HCO_3^- was observed in the ^{13}C-NMR (see Fig. S11 in the ESM), suggesting the CO_2 capture at the $–O^-TBA^+$ sites. To further understand the interaction of CO_2 with the MOF, their CO_2 adsorption energy and volume adsorbed were estimated from the CO_2 physisorption isotherms, employing the Dubinin–Radushkevich equation (see Fig. S12 in the ESM). Similar adsorption energies were obtained for both the neutral and ionic MOFs (13 vs. 11 $kJ·mol^{-1}$, respectively), indicating a similar CO_2 physisorption at the Zn-O sites (see Table S11 in the ESM). However, the amount of CO_2 physisorbed was higher for the (more porous) neutral MOF (1.7 vs. 0.1 $mmol·g^{-1}$), in line with the N_2 sorption capacity (surface area, pore size, and volume).

Given the high activity of isoreticular MOF-74 catalysts for this reaction, i.e., Co-MOF-74 [15], the CO_2 cycloaddition to epichlorohydrin was tested using TBABr by itself or in the presence of the three Na@M_2(dot) MOFs. The product starts forming appreciably after 0.5 h of reaction and reaches full yield after 3 h (see left part of Fig. 2(b) and Fig. S13 in the ESM). A twofold increase in reaction rate (calculated as mmol of epichlorohydrin converted to the cyclic carbonate per hour of reaction) is observed in the presence of the MOF, passing from 0.40 $mmol·h^{-1}$ (in the absence of any MOF) to 0.84 $mmol·h^{-1}$ for Zn_2(dot), 0.78 $mmol·h^{-1}$ for Ni_2(dot), and 0.92 $mmol·h^{-1}$ for Co_2(dot). This further proves the activity of the neutral MOF catalyst in the reaction, cooperatively activating the reagents together with the TBABr co-catalyst. Contrary to the best performant Zn-MOF proposed in the Refs. [13, 19], the higher catalytic activity of Co and Ni might be due to their lower particle size and higher number of defects, as proved by XRD and XPS.

The TOF attributed only to the Lewis acid (i.e., MOF) can be estimated by subtracting the yield of cyclic carbonate obtained with the metal-containing catalyst (i.e., the MOF) from the yield obtained using only TBABr (both after 1 h reaction to account for

initial reaction rates at low conversions), and dividing this difference by the catalyst concentration and reaction time [25]. We have estimated TOFs of 10–15 h^{-1} for the Lewis acid sites in the Na@M_2(dot) MOFs (in the presence of the TBABr co-catalyst) using this approach (see Table S10 in the ESM), which suggests a considerable catalytic activity of the MOF Lewis acid sites (in addition to the nucleophilic and Lewis base TBABr co-catalyst). The TOF estimated Co (14 h^{-1}) > Zn (13 h^{-1}) > Ni (10 h^{-1}) are higher than those reported for similar combinations of MOF-IL [14]. However, the catalytic activity of the MOFs is not only a result of the Lewis acid strength (charge/radii ratio) of the M^{2+} ions present in the MO_6 octahedral secondary building units (SBUs) of the MOF (with radius of 0.65, 0.69, and 0.74 Å, for Co^{2+}, Ni^{2+}, and Zn^{2+}, respectively) [26]. The number of coordinatively unsaturated sites, particle size, and TBABr loading (and the water associated to both metal cation and ionic liquid) should be taken into account, all promoting the diffusion and reaction steps [27]. It is worth mentioning that no further TBABr additive (co-catalyst) was employed during the recycling of the Na@M_2dot materials, and that a similar amount of epichlorohydrin was injected into the reaction vessel containing the spent MOF.

In the case of the TBA@M_2(dot) ionic MOFs with confined TBABr, their catalytic activity is much higher than the Na@M_2(dot) neutral MOFs in the absence of TBABr as a co-catalyst (see right part of Fig. 2(b)). In contrast with the limited activity of Na@M_2(dot) neutral MOFs, close to 60% yield of cyclic carbonate is obtained after just 3 h with all three TBA@M_2(dot) ionic MOFs. The yield after 1 h (related to the catalytic activity) is higher for the ionic Zn MOF, probably due to the higher amount of ionic liquid incorporated, with respect to the Ni and Co ionic MOFs. Figure 2(c) shows a slight decrease in yield obtained after 3 h for both Na@M_2(dot) or TBA@M_2(dot) MOFs, which in any case is higher than that obtained with the control reaction for the same reaction time. This indicates the adequate immobilization of the TBABr, either post-synthesis (for the Na@M_2(dot) samples) or directly formed within the MOF structure (for the TBA@M_2(dot) samples). Moreover, the crystalline structure of the metal-dioxyterephthalate is maintained after three reaction cycles, albeit some changes in the intensity of the two main low-angle diffraction signals are observed (at ca. 6.7° and 11.7°), especially for the Co MOF (see Fig. S14 in the ESM). In all of them, the relative intensity of the first peak (corresponding to the (011) plane) with respect to the second one (corresponding to the (300) plane) decreases, indicating the blocking of the larger pores by confined TBABr. Interestingly, the broadness of the XRD peaks is similar before and after the reaction, suggesting minor changes in particle size under the reaction conditions. The FTIR spectra of the MOFs before and after the catalytic test in the presence of TBABr suggest that the metal carboxylate (1550 and 1400 cm^{-1}) bands are maintained during the reaction (see Fig. S15 in the ESM), with an increase in the band around 3000–3500 cm^{-1}, suggesting the presence of TBABr. Elemental analysis suggested a decrease in the nitrogen amount in the samples after the second reuse, especially for the Zn-containing one, which may account for the activity decrease of the spent ionic MOF (see Table S3 in the ESM). A similar activity decrease is observed upon activation of the TBA@Zn_2(dot) by soaking it in methanol at room temperature for one week (see Fig. S16 in the ESM).

Considering the metal content obtained by TGA in the TBA@M_2(dot), the TOFs are 59, 26, and 12 h^{-1} while the TONs are 195, 121, and 71, for the Zn, Ni, and Co ionic MOFs (see right part of Fig. 2(d)). Those values are one order of magnitude higher than the TOF = 1 h^{-1} obtained for bare Na@M_2(dot). Since the co-catalyst exhibits much higher activity than the metal sites, the amount of nitrogen in the material (obtained from combustion analysis) was considered as the active site, assuming to be the same amount of TBABr (having one equivalent of N). Figure 2(d) shows that all the TBA@M_2(dot) samples (right part) have a TON 2–6 times higher than the TON obtained in the case of using TBABr as the sole catalyst. Therefore, the TBA species were key in the catalytic activity of the material, either having bromide or acetate counterions. Both TONs and TOFs obtained with the nitrogen amount are higher than those for the metal, highlighting the effect of choosing a particular active site for the calculation of the TOF [25].

The separate activity of either the TBA^+ or the Br^- species in the MOF was studied (see Fig. S17 in the ESM). On the one hand, a sample with TBA^+ and no Br^- was prepared using $Zn(OAc)_2$ as the metal source and TBAOH as the base to deprotonate the linker (see TBAOAc@Zn_2(dot) in Scheme 2(a_2)). This MOF-IL composite still exhibits 75% of the catalytic activity of the TBA@Zn_2(dot) (named as TBABr@Zn_2(dot) in Scheme 2(b_2)). Bulkier alkyl ammonium hydroxide bases, such as cetyltrimethylammonium hydroxide (CTAOH) have been employed to deprotonate the dot linker and form the MOF-IL upon reaction with the $ZnBr_2$ salt. Despite the incorporation of the CTABr within the MOF structure (see XRD, FTIR, and TGA in Fig. S18 in the ESM), the catalytic activity was not improved with respect to using TBAOH as the base (see Figs. S17 and S18 in the ESM). Interestingly, the XRD pattern of TBAOAc@Zn_2(dot) indicates the increase in the broadness of the peaks and the displacement of the first peak (corresponding to the (011) plane) towards smaller angles (0.57° with respect to NaOAc@Zn_2(dot) and 0.35° with respect to TBABr@Zn_2(dot)), compared with TBAAc@Zn_2(dot), as shown in Fig. S18(b) in the ESM. This indicates microstrains due to defects in the MOF nanocrystals and the increase in the cell parameters. The bulky and basic TBAOAc ionic liquid seems to favor the generation of dense phases probably corresponding to ZnO/ZnOH nanoparticles, as indicated by new peaks appearing at higher angles. On the other hand, a sample with Na^- and Br^- was prepared using $ZnBr_2$ as the metal source and NaOH as the base to deprotonate the linker (see NaBr@Zn_2(dot) in Scheme 2(b_1)). This MOF exhibits negligible catalytic activity, like the Na@Zn_2(dot) (named as NaOAc@Zn_2(dot) in Scheme 2(a_1)).

Based on the catalytic activity of the O-defect-containing MOFs, a tentative mechanism involving the participation of carboxylate (pKa COOH of ca. 5) and/or phenolate groups (pKa OH of ca. 10) [28], can be proposed (see Scheme S1 in the ESM). In the case of Co-MOF-74, in the literature it is proposed that the binding of CO_2 to the alkoxide oxygen increases the flexibility of the substrate moiety, enabling the cyclization pathway in which CO_2 is incorporated into the final product [24, 28]. Indeed, the physisorption of CO_2 with energies of 11–13 kJ·mol^{-1} in both ionic and neutral Zn-MOF (see Table S12 in the ESM), as well as the reaction rate dependence with CO_2 pressure for the TBA@Zn_2(dot) ionic MOF (see Fig. S19 in the ESM) indicates the participation of CO_2 in the rate-limiting step of the reaction mechanism. In addition, a parallel trend between the reaction rate and the epichlorohydrin concentration is observed for TBA@Zn_2(dot), further suggesting the bimolecular mechanism of the cycloaddition reaction involving this ionic MOF as catalyst. Thus, both basic

oxygen groups and acid under coordinated metal sites participate as Lewis acid-base pairs in activating both reactants (CO_2 and epoxide) and adsorbing the TBABr co-catalyst. As described above, the XPS red shift in the case of the TBABr containing MOF further suggests the presence of Br anions close to the Zn sites, as depicted in Scheme S1 in the ESM. Based on the kinetic experiments performed, pathway (b) where the active site is the occluded TBABr is more favored than pathway (a), given the differences in TON and TOFs of 1–3 orders of magnitude when considering each active site for its calculation.

To further support the higher activity of TBA@Zn_2(dot) with respect to Na@Zn_2(dot), the CO_2 cycloaddition to epichlorohydrin has been performed at different temperatures to estimate the activation energy from the changes in the reaction rate and TOF. Apparent activation energies of 20 kJ·mol^{-1} were obtained for both homogeneous TBABr and heterogeneous TBA@Zn_2(dot), while close to 120 kJ·mol^{-1} was needed in the case of Na@Zn_2(dot). The lower activation energy and pre-exponential factor indicate a better stabilization (and stronger interaction) of the CO_2 and epichlorohydrin substrates in the TBA-containing catalyst. Similar values of activation enthalpy (17 vs. 116 kJ·mol^{-1}) were obtained when the Eyring plot was used instead of the Arrhenius one (see Table S12 and Fig. S20 in the ESM). Besides the lower activation enthalpies obtained in the presence of TBABr (either in bulk or grafted to the MOF), the Eyring plot provides much lower activation entropies, which again suggests a higher interaction-activation of reagents when the nucleophilic TBA sites are present in addition (and possibly cooperatively) to the zinc Lewis acid sites.

Table 1 highlights that the novel TBA@M_2(dot) ionic MOFs reported herein (in the absence of TBABr additive and under atmospheric CO_2 pressure) are competitive or even better than reported MOFs containing similar ammonium bromide active sites either as additive (TONs of ca. 10–50) or grafted to the porous materials (TONs 10–1000) [16–18, 20, 29–40]. Finally, the benchmark ionic TBA@Zn_2(dot) catalyst has been evaluated in the CO_2 cycloaddition of different epoxides. Quantitative conversion of epichlorohydrin, styrene oxide, glycidol, and glycidyl methacrylate was obtained at 80 °C (CO_2 balloon) under solvent-free and additive-free conditions (see Figs. S21–S24 in the ESM), indicating the general applicability of the ionic MOF. We believe that the promising performance of this novel ionic MOF on CO_2 cycloaddition reactions will contribute to greenhouse gas and pollutant CO_2 capture and conversion in the near future [41, 42].

3 Conclusions

A novel approach towards ionic MOFs containing nucleophilic active sites such as Br^- is proposed here for the first time, employing first-row divalent transition metals (i.e., Zn, Ni, and Co) and green synthesis conditions using water at ambient conditions. We show the key role of the base and metal salt employed in the MOF synthesis, allowing the formation of ionic liquids within the MOF structure in the case of using metal bromides and alkyl ammonium bases as deprotonating and directing agents of both linkers and

Table 1 Metal content and catalytic performance of the Na/TBA@M_2(dot) with respect to benchmark MOF-ionic liquid catalysts

Refs.	TBABr	MOF	P_{CO2} (bar)	T (°C)	t (h)	Yield (%)	TON[a]
This work	Yes (0.4 mol%)	none	1	80	3	52	—
	No	Na@Zn_2(dot)				76	155
		Na@Ni_2(dot)				86	175
		Na@Co_2(dot)				85	173
		None				1	—
		TBA@Zn_2(dot)				66	366
		TBA@Ni_2(dot)				65	443
		TBA@Co_2(dot)				48	709
[16]	No	Co-MOF-74	20	100	4	96	46[c]
[17]	Yes (10 mol%)	Co(II)-NDC MOF	1	80	12	90	10
[18]	Yes (3 mol%)	Ni(salphen)- MOF	20	80	4	84	28
[20]	Yes (3.75 mol%)	ZnMOF	12	RT	60	99	26
[29]	Yes (1.5 mol%)	Zn-MOF-184	1	80	6	72	48
[30]	No	AMIMBr@H2P-DHPh COF	10	120	24	91	1131[b]
[32]	No	IL-UiO-67	1	90	12	95	63
[33]	No	PIL-4@MIL-101-0.25	10	90	2.5	87	38[c]
[34]	No	polyIL-MIL-101	1	70	24	90	9[c]
[35]	No	Pyridinium/triazolium-MIL101	10	120	2	95	155[d]
[36]	No	MIL-101-tz-TMA-Br	10	80	1	90	177[d]
[37]	No	IL@MIL-101-SO_3H	1	90	48	98	302[c]
[38]	Yes (6 mol%)	NUC-82(Co)	1	65	4.5	97	198
[39]	Yes (1.5 mol%)	NUC-103(In, Cd)	5	65	5	99	1042
[40]	Yes (5 mol%)	NUC-111a(Pd)	9	75	4	99	1800

[a] Based on the mols of N from the ammonium bromide, determined by elemental analysis. [b] Based on the mols of grafted 1-methyl imidazolium bromide. [c] Based on the mols of N, determined by elemental analysis. [d] Based on the mols of Br, determined by Br^- chromatography.

final MOF nanocrystals. The structure and composition have been thoroughly characterized using different techniques such as XRD, SEM, FTIR, TGA, XPS, and elemental analysis. These TBA@M_2dot ionic-liquid/MOF hybrid materials can promote the CO_2 cycloaddition to epoxide with TONs of the confined TBABr up to 700, exhibiting adequate ionic liquid-MOF interactions which allow for use as a heterogeneous catalyst during different reaction cycles with minor decrease in catalytic activity. The proposed materials allow employing at least ten times less TBABr (i.e., 0.3 wt.%), and less than 1 wt.% of metal (0.7 wt.%–0.9 wt.%) with respect to the epoxide at just 1 bar of CO_2 (balloon).

Electronic Supplementary Material: Supplementary material (material synthesis, characterization, and catalytic performance) is available in the online version of this article at https://doi.org/10.26599/NR.2025.94907069.

Data availability

All data needed to support the conclusions in the paper are presented in the manuscript and the Electronic Supplementary Material. Additional data related to this paper may be requested from the corresponding author upon request.

Acknowledgments

F. G. C. and N. M. acknowledge the "Ramon y Cajal" contract with code RYC2020-028681-I and RYC2021-033167-I funded MCIN/AEI/10.13039/501100011033 and by "ESF investing in your future", "European Union NextGenerationEU/PRTR". This work has been partially supported by MICINN-FEDER-AEI 10.13039/501100011033 (PID2021-124695OB-C22, PID2022-142897OA-I00), MCIN/AEI/10.13039/501100011033 and by the European Union Next Generation EU-PRTR (TED2021-129626B-I00 and TED2021-130288B-I00). F. G. C. thanks Generalitat Valenciana (CISEJI/2023/78). UJI is acknowledged for the project UJI-2023-03.

Declaration of competing interest

There are no conflicts to declare.

Author contribution statement

N. M.: Conceptualization, funding acquisition, data curation, formal analysis, investigation, methodology, writing – original draft, writing – review & editing. M. M.-P.: Investigation, writing – review & editing. J. S. V.: Methodology. B. A.: Investigation, writing – review & editing. E. G.-V.: Formal analysis, funding acquisition, investigation, methodology, writing – review & editing. F. G. C.: Conceptualization, formal analysis, funding acquisition, investigation, methodology, supervision, writing – original draft, writing – review & editing.

Use of AI statement

None.

References

[1] Kitagawa, S.; Kitaura, R.; Noro, S. I. Functional porous coordination polymers. *Angew. Chem., Int. Ed.* **2004**, *43*, 2334–2375.

[2] Diercks, C. S.; Yaghi, O. M. The atom, the molecule, and the covalent organic framework. *Science* **2017**, *355*, eaal1585.

[3] Villa, R.; Alvarez, E.; Porcar, R.; Garcia-Verdugo, E.; Luis, S. V.; Lozano, P. Ionic liquids as an enabling tool to integrate reaction and separation processes. *Green Chem.* **2019**, *21*, 6527–6544.

[4] Luo, Q. X.; An, B. W.; Ji, M.; Zhang, J. Hybridization of metal-organic frameworks and task-specific ionic liquids: Fundamentals and challenges. *Mater. Chem. Front.* **2018**, *2*, 219–234.

[5] Kinik, F. P.; Uzun, A.; Keskin, S. Ionic liquid/metal-organic framework composites: From synthesis to applications. *ChemSusChem* **2017**, *10*, 2842–2863.

[6] Durak, O.; Zeeshan, M.; Habib, N.; Gülbalkan, H. C.; Moqbel Alsuhile, A. A.; Çağlayan, H. P.; Kurtoğlu-Öztulum, S. F.; Zhao, Y. X.; Haşlak, Z. P.; Uzun, A. et al. Composites of porous materials with ionic liquids: Synthesis, characterization, applications, and beyond. *Microporous Mesoporous Mater.* **2022**, *332*, 111703.

[7] Rosenboom, J. G.; Langer, R.; Traverso, G. Bioplastics for a circular economy. *Nat. Rev. Mater.* **2022**, *7*, 117–137.

[8] Santacesaria, E.; Tesser, R.; Di Serio, M.; Casale, L.; Verde, D. New process for producing epichlorohydrin via glycerol chlorination. *Ind. Eng. Chem. Res.* **2010**, *49*, 964–970.

[9] Wang, Y. W.; Zhu, X. H.; Zhang, Y.; Yuan, D.; Yao, Y. M. Synthesis and characterization of cobalt(II/II) and cobalt(II/III) macrocyclic complexes and their application in the copolymerization of epoxides and CO_2. *Organometallics* **2023**, *42*, 1579–1588.

[10] Yin, K.; Hua, L. Y.; Qu, L. Y.; Yao, Q. Y.; Wang, Y. R.; Yuan, D.; You, H. P.; Yao, Y. M. Heterobimetallic rare earth metal-zinc catalysts for reactions of epoxides and CO_2 under ambient conditions. *Dalton Trans.* **2021**, *50*, 1453–1464.

[11] Grant Glover, T.; Peterson, G. W.; Schindler, B. J.; Britt, D.; Yaghi. O. MOF-74 building unit has a direct impact on toxic gas adsorption. *Chem. Eng. Sci.* **2011**, *66*, 163–170.

[12] Zheng, J.; Vemuri, R. S.; Estevez, L.; Koech, P. K.; Varga, T.; Camaioni, D. M.; Blake, T. A.; McGrail, B. P.; Motkuri, R. K. Pore-engineered metal-organic frameworks with excellent adsorption of water and fluorocarbon refrigerant for cooling applications. *J. Am. Chem. Soc.* **2017**, *139*, 10601–10604.

[13] Choe, J. H.; Kim, H.; Hong, C. S. MOF-74 type variants for CO_2 capture. *Mater. Chem. Front.* **2021**, *5*, 5172–5185.

[14] Tapiador, J.; García-Rojas, E.; López-Patón, P.; Calleja, G.; Orcajo, G.; Martos, C.; Leo, P. Influence of divalent metal ions on CO_2 valorization at room temperature by isostructural MOF-74 materials. *J. Environ. Chem. Eng.* **2023**, *11*, 109497.

[15] Sánchez-Sánchez, M.; Getachew, N.; Díaz, K.; Díaz-García, M.; Chebude, Y.; Díaz, I. Synthesis of metal-organic frameworks in water at room temperature: Salts as linker sources. *Green Chem.* **2015**, *17*, 1500–1509.

[16] Cho, H. Y.; Yang, D. A.; Kim, J.; Jeong, S. Y.; Ahn, W. S. CO_2 adsorption and catalytic application of Co-MOF-74 synthesized by microwave heating. *Catal. Today* **2012**, *185*, 35–40.

[17] Chand, S.; Pal, S. C.; Mondal, M.; Hota, S.; Pal, A.; Sahoo, R.; Das, M. C. Three-dimensional Co(II)-metal-organic frameworks with varying porosities and open metal sites toward multipurpose heterogeneous catalysis under mild conditions. *Cryst. Growth Des.* **2019**, *19*, 5343–5353.

[18] Ren, Y. W.; Shi, Y. C.; Chen, J. X.; Yang, S. R.; Qia, C. R.; Jiang, H. F. Ni(salphen)-based metal-organic framework for the synthesis of cyclic carbonates by cycloaddition of CO_2 to epoxides. *RSC Adv.* **2013**, *3*, 2167–2170.

[19] Ma, M. Y.; Zacher, D.; Zhang, X. N.; Fischer, R. A.; Metzler-Nolte, N. A method for the preparation of highly porous, nanosized crystals of isoreticular metal-organic frameworks. *Cryst. Growth Des.* **2011**, *11*, 185–189.

[20] Zou, R. Y.; Li, P. Z.; Zeng, Y. F.; Liu, J.; Zhao, R.; Duan, H.; Luo, Z.; Wang, J. G.; Zou, R. Q.; Zhao, Y. L. Bimetallic metal-organic

frameworks: Probing the Lewis acid site for CO_2 conversion. *Small* **2016**, *12*, 2334–2343.

[21] Heidary, N.; Chartrand, D.; Guiet, A.; Kornienko, N. Rational incorporation of defects within metal-organic frameworks generates highly active electrocatalytic sites. *Chem. Sci.* **2021**, *12*, 7324–7333.

[22] Yang, D. A.; Cho, H. Y.; Kim, J.; Yang, S. T.; Ahn, W. S. CO_2 capture and conversion using Mg-MOF-74 prepared by a sonochemical method. *Energy Environ. Sci.* **2012**, *5*, 6465–6473

[23] Das, P.; Mandal, S. K. Unprecedented high temperature CO_2 selectivity and effective chemical fixation by a copper-based undulated metal-organic framework. *ACS Appl. Mater. Interfaces* **2020**, *12*, 37137–37146.

[24] Xu, K.; Moeljadi, A. M. P.; Mai, B. K.; Hirao, H. How does CO_2 react with styrene oxide in Co-MOF-74 and Mg-MOF-74. Catalytic mechanisms proposed by QM/MM calculations. *J. Phys. Chem. C* **2018**, *122*, 503–514.

[25] Campisciano, V.; Calabrese, C.; Giacalone, F.; Aprile, C.; Lo Meo, P.; Gruttadauria, M. Reconsidering TOF calculation in the transformation of epoxides and CO_2 into cyclic carbonates. *J. CO_2 Util.* **2020**, *38*, 132–140.

[26] Shannon, R. D. Revised effective ionic radii and systematic studies of interatomic distances in halides and chalcogenides. *Acta Cryst.* **1976**, *A32*, 751–767.

[27] Valverde, D.; Porcar, R.; Lozano, P.; García-Verdugo, E.; Luis, S. V. Multifunctional polymers based on ionic liquid and rose bengal fragments for the conversion of CO_2 to carbonates. *ACS Sustain. Chem. Eng.* **2021**, *9*, 2309–2318.

[28] Alassmy, Y. A.; Pescarmona, P. P. The role of water revisited and enhanced: A sustainable catalytic system for the conversion of CO_2 into cyclic carbonates under mild conditions. *ChemSusChem* **2019**, *12*, 3856–3863.

[29] Tran, Y. B. N.; Nguyen, P. T. K.; Luong, Q. T.; Nguyen, K. D. Series of M-MOF-184 (M = Mg, Co, Ni, Zn, Cu, Fe) metal-organic frameworks for catalysis cycloaddition of CO_2. *Inorg. Chem.* **2020**, *59*, 16747–16759.

[30] Zhang, Y.; Hu, H.; Ju, J.; Yan, Q. Q.; Arumugam, V.; Jing, X. C.; Cai, H. Q.; Gao, Y. N. Ionization of a covalent organic framework for catalyzing the cycloaddition reaction between epoxides and carbon dioxide. *Chin. J. Catal.* **2020**, *41*, 485–493.

[31] Ding, L. G.; Yao, B. J.; Jiang, W. L.; Li, J. T.; Fu, Q. J.; Li, Y. A.; Liu, Z. H.; Ma, J. P.; Dong Y. B. Bifunctional imidazolium-based ionic liquid decorated UiO-67 type MOF for selective CO_2 adsorption and catalytic property for CO_2 cycloaddition with epoxides. *Inorg. Chem.* **2017**, *56*, 2337–2344.

[32] Jiang, Y. C.; Zhao, Y. F.; Liang, L.; Zhang, X.; Sun, J. M. Imidazolium-based poly(ionic liquid)s@MIL-101 for CO_2 adsorption and subsequent catalytic cycloaddition without additional cocatalyst and solvent. *New J. Chem.* **2022**, *46*, 2309–2319.

[33] Ding, M. L.; Jiang, H. L. Incorporation of imidazolium-based poly(ionic liquid)s into a metal-organic framework for CO_2 capture and conversion. *ACS Catal.* **2018**, *8*, 3194–3201.

[34] Liu, W. S.; Zhou, L. J.; Li, G.; Yang, S. L.; Gao, E. Q. Double cationization approach toward ionic metal-organic frameworks with a high bromide content for CO_2 cycloaddition to epoxides. *ACS Sustain. Chem. Eng.* **2021**, *9*, 1880–1890.

[35] Xiong, L. F.; Zhou, L. J.; Bu, R.; Yang, S. L.; Gao, E. Q. Efficient ionic functionalization of metal-organic frameworks for efficient addition of carbon dioxide to epoxides. *Microporous Mesoporous Mater.* **2022**, *330*, 111601.

[36] Sun, Y. X.; Jia, X. M.; Huang, H. L.; Guo, X. Y.; Qiao, Z. H.; Zhong, C. L. Solvent-free mechanochemical route for the construction of ionic liquid and mixed-metal MOF composites for synergistic CO_2 fixation. *J. Mater. Chem. A* **2020**, *8*, 3180–3185.

[37] Sun, Y. X.; Huang, H. L.; Vardhan, H.; Aguila, B.; Zhong, C. L.; Perman, J. A.; Al-Enizi, A. M.; Nafady, A.; Ma, S. Q. Facile approach to graft ionic liquid into MOF for improving the efficiency of CO_2 chemical fixation. *ACS Appl. Mater. Interfaces* **2018**, *10*, 27124–27130.

[38] Zhang, X. T.; Wang, X. T.; Li, C.; Hu, T. P.; Fan, L. M. Nanoporous $\{Co_3\}$-Organic framework for efficiently seperating gases and catalyzing cycloaddition of epoxides with CO_2 and Knoevenagel condensation. *J. Colloid Interface Sci.* **2024**, *656*, 127–136.

[39] Zhang, X. T.; Wang, X. T.; Li, C.; Fan, L. M.; Hu, T. P. Robust heterometallic $\{In_2CdO\}$-Organic framework for efficiently catalyzing CO_2 cycloaddition and Knoevenagel condensation. *Sep. Purif. Technol.* **2025**, *354*, 128926.

[40] Zhao, B.; Li, C.; Hu, T. P.; Gao, Y. P.; Fan, L. M.; Zhang, X. T. Robust $\{Pb_{10}\}$-cluster-based metal-organic framework for capturing and converting CO_2 into cyclic carbonates under mild conditions. *Inorg. Chem.* **2024**, *63*, 14183–14192.

[41] Han, C.; Zhang, X. D.; Huang, S. S.; Hu, Y.; Yang, Z.; Li, T. T.; Li, Q. P.; Qian, J. J. MOF-on-MOF-derived hollow Co_3O_4/In_2O_3 nanostructure for efficient photocatalytic CO_2 reduction. *Adv. Sci.* **2023**, *10*, 2300797.

[42] Dong, A. R.; Chen, D. D.; Li, Q. P.; Qian, J. J. Metal-organic frameworks for greenhouse gas applications. *Small* **2023**, *19*, 2201550.